RSC Advances

PAPER

View Article Online
View Journal | View Issue

Cite this: *RSC Adv.*, 2026, **16**, 6394

Visible-light-responsive Fe_2O_3–TiO_2–carbon dot nanocomposite coatings for enhanced biofouling mitigation in aquaculture cage nets

R. Gopika[ab] and P. Muhamed Ashraf *[a]

A photocatalytic antifouling coating was designed for aquaculture cage nets, as biofouling is a persistent challenge in aquaculture that substantially reduces operational efficiency and compromises the economic performance of the systems. A nanostructured composite was developed using nano-titanium dioxide (TiO_2), iron(III) oxide (Fe_2O_3), and carbon dots (CDs). The antifouling efficacy of the composite was evaluated by applying it onto a (3-glycidyloxypropyl)trimethoxysilane (silane)-pretreated polyethylene substrate, followed by immersion in natural estuarine waters. This ternary photocatalytic composite, formed by the interaction between the C=C bond of CDs and inorganic oxides, exhibited a reduced band gap from 4 eV to 1.7 eV by suppressing electron–hole recombination. The uniform distribution in the composite was evidenced by XRD, the characteristic peaks of TiO_2 and Fe_2O_3 suggested nanoscale crystallinity, and the $2\theta = 21°$ peak suggested the presence of low-crystalline CDs in the matrix, which was confirmed by transmission electron microscopy. The nanocomposite uniformly coated over silane-pretreated polyethylene exhibited strong interfacial bonding between CD aromatic moieties and glycidyloxy C–O–C groups. Nets coated with a 0.05% FeTiCD nanocomposite exhibited excellent biofouling resistance in a six-month field trial. Fe(III) doping introduced mid-gap states, enabling efficient electron transfer to CDs and sustained reactive oxygen species (ROS) production, thereby disrupting the attachment of biofouling organisms. This nanocomposite offers a scalable, low-impact antifouling solution that supports more sustainable aquaculture operations.

Received 1st December 2025
Accepted 16th January 2026

DOI: 10.1039/d5ra09273f

rsc.li/rsc-advances

1 Introduction

Photocatalysts are materials that enhance the rate of a chemical reaction upon exposure to light by initiating active oxidation and reduction reactions.[1] These materials produce reactive oxygen species (ROS), which act as potent oxidizing agents capable of degrading toxic organic compounds and disinfecting bacteria.[2] Titanium dioxide (TiO_2) is a widely recognized semiconductor and a potential photocatalyst owing to its unique properties, such as photostability, low cost and nontoxic nature.[3] The anatase phase of bulk TiO_2 has a band gap of 3.2 eV, restricting its response to UV radiation and thus limiting sunlight absorption (5–7%).[3,4] Additionally, it exhibits rapid electron–hole (e^-/h^+) recombination, a low quantum yield and reduced adsorption efficiency, resulting in poor photocatalytic efficiency.[5]

The photocatalytic efficiency of TiO_2 can be enhanced by integrating it with transition metals and carbon nanomaterials such as carbon nanotubes (CNTs), fullerenes and graphene,[6–8] which delay e^-/h^+ recombination. Transition metals induce Schottky and plasmonic effects, while carbon nanomaterials offer a high specific surface area and electrical mobility.[9–14] Carbon nanomaterials can also form additional energy levels, reduce the band gap and increase sensitivity to visible light.[3] Carbon dots (CDs) are synthesized from natural raw materials, are resistant to photobleaching, and possess low toxicity, high chemical and photostability, excellent biocompatibility, and cost-effectiveness.[15–17] Thus, CDs can be integrated into TiO_2 to enhance the photocatalytic activity of TiO_2. Fe^{3+} oxide, possessing a $3d^5$ configuration, initiates photocatalysis by releasing and facilitating the migration of trapped carriers. It also narrows the band gap, creating intermediate energy levels, and delays e^-/h^+ recombination. The doping of Fe^{3+} into TiO_2 extends its photocatalytic activity from the UV to visible region.[18,19] Not many studies have reported the integration of CDs, iron oxide and TiO_2 to produce photocatalytic materials with reduced band gaps and delayed e^-/h^+ recombination.

The accumulation of undesirable micro- and macro-organisms on submerged structures, such as ship hulls and offshore platforms, is referred to as biofouling. In aquaculture, the biofouling of cage nets is a significant and widely recognized issue, impacting farm productivity, fish health, and maintenance costs. According to the FAO (2024), the global

[a]ICAR-Central Institute of Fisheries Technology, Matsyapuri PO, Cochin 682 029, Kerala, India. E-mail: ashrafp2008@gmail.com; Fax: +91 484 2668212; Tel: +91 484 2412300; +91 9746236477

[b]Cochin University of Science and Technology, Cochin 682 022, Kerala, India

aquaculture production reached 130.9 million tonnes in 2022, of which 94.4 million tonnes comprised aquatic animals. To meet the growing demand for aquatic food, the FAO emphasizes the need for sustainable intensification and expansion of aquaculture. Implementing effective antifouling strategies by employing nanomaterial-based advanced coatings is crucial for maintaining optimal aquaculture operations while minimizing environmental impact. To combat biofouling, the surface modification of submerged surfaces with antimicrobial agents is among the most effective methods. Nano-sized biocides employed for the antifouling of aquaculture cage nets include cuprous oxide,[20] ZnO,[21] ZnO–SiO composites,[22] nanocarbon–inorganic biocide composites, nitrogen-doped CDs,[23] and photocatalytic nano-TiO_2-based composites,[24,25] all of which have shown significantly enhanced antifouling properties.

The nonpolar surface of polyethylene does not adsorb biocides effectively without prior surface modification.[25] Organosilicon-based sol–gel materials like silane are widely used for surface modification of textiles due to their hydrophobicity, chemical stability, self-cleaning ability, nontoxicity, enhanced surface durability, and resistance to ice formation.[26–31] These properties make them potential materials for surface modification of nonpolar surfaces like PE. Ashraf *et al.* reported the utilization of organosilicon molecules to modify the polyalkene surfaces.[25] In recent years, photocatalytic activity and its application are attracting attention for the development of biocidal molecules. TiO_2 codoped with Ag, carbon and sulfur; ZnO with concrete; graphitic carbon nitrite; Cd sulfide with reduced graphene oxide; Zr_6Ti_4-based metal–organic frameworks; and ZnO reduced graphene oxide coatings have been widely utilized as biocides across various sectors including healthcare, construction, and water treatment plants.[31–37] Very few studies have been attempted to develop antifouling strategies for aquaculture cage nets using photocatalytic materials as biocides. Synthesis of a Fe_2O_3–TiO_2–CD (FeTiCD) nano composite with improved biocidal properties, expected to produce more reactive oxygen species (ROS) for inhibiting microorganism growth, and its application as an effective antifouling biocide in aquatic environment. The photocatalytic efficiency of TiO_2 doped with Fe_2O_3 degrade organic biofouling agents, antimicrobial and light harvesting activity of CD prevent microbial colonization even in natural condition. Ashraf *et al.* (2024) reported the CuO–TiO_2–CD composite, which has a similar synthetic route as the FeTiCD composite.[25] Copper oxide nanoparticles are toxic in nature, and they can cause oxidative stress, inflammation, cytotoxicity, genotoxicity and immunotoxicity in living systems.[38] Therefore, Fe_2O_3 is selected instead of CuO for the synthesis of the FeTiCD ternary system owing to its lower toxicity, economic viability, and eco-friendly nature. Excellent photocatalytic activity and a reduced band gap are obtained when Fe_2O_3 is doped into TiO_2.[39,40] Fe_2O_3 is considered an ideal dopant for TiO_2 owing to its magnetic properties and low band gap energy, and Fe_2O_3–TiO_2 shows excellent persistent organic pollutant removal and better photocatalyst recovery.[41] The band gaps reported for the CuO–TiO_2 nanocatalyst and carbon-doped TiO_2/CuO photocatalyst are 2.8 and 2.2–2.5 eV, respectively.[42,43] The band gap energy of the photocatalyst proposed here is much better than that of the CuO-doped TiO_2 photocatalyst. Most of the existing photocatalytic systems of Fe and Ti are used for the removal of pollutants in water treatment plants, organic dye degradation, and so forth, but here, we use them as an antifouling coating for aquaculture cage nets to prevent biofouling. In contrast to biocide coatings like CuO, the presented coating is a sustainable and nontoxic approach. Hence, this synergistic coating can enhance the antifouling property under sunlight through the continuous supply of reactive oxygen species (ROS).

Herein, we propose the facile synthesis of a FeTiCD nanocomposite through hydrothermal carbonization using in-house-synthesized fish skin-derived carbon dots.[44] Capitalizing on the efficient light-harvesting capabilities of CDs, the resulting FeTiCD composite coated on a silane base shows significant promise as an antifouling agent for polyethylene aquaculture cage nets. This innovative approach aims to enhance the efficacy of antifouling strategies, addressing the critical issue of biofouling in aquaculture systems.

2 Materials and methods

2.1. Materials used

Nano-iron oxide (Fe_2O_3) (5 wt% solution), a titanium dioxide (anatase) photocatalyst nanopowder having a size of approximately 7 nm, dimethyl sulfoxide and (3-glycidyloxypropyl)trimethoxysilane (silane), respectively, were procured from Plasma Chem GmbH, Berlin, SRL Chemicals, India, Qualigens, India, and Sigma-Aldrich. High-density polyethylene (HDPE) was obtained from the Government's Matsyafed Net Factory, Kochi, India. MilliQ type 1 water was used throughout the analysis. The polyethylene cage nets were pretreated using organosilane as per the method described by Ashraf *et al.*[25]

2.2. Synthesis and characterization of the photocatalytic Fe_2O_3–TiO_2–CD nanocomposite

Initially, the nano-Fe_2O_3 and TiO_2 composite (FeTi) was synthesized through a hydrothermal method.

0.20 g of nano-Fe_2O_3, 0.10 g of TiO_2 (2 : 1), 1 mL of dimethyl sulfoxide (DMSO) and 20 mL of water were taken in a 100 mL Teflon vessel. DMSO acted as a stabilizing agent, preventing nanoparticle aggregation and maintaining dispersion stability.[45] The mixture was then subjected to hydrothermal synthesis with a temperature program of 1 hour to reach 180 °C, followed by 2 hours at 180 °C. After allowing it to cool naturally, the formed FeTi composite was centrifuged and washed thoroughly with MilliQ type 1 water at least three times. The residue was separated and dried. To incorporate CDs into this synthesized FeTi composite, the composite and CDs were mixed in a 2 : 1 (w/w) weight ratio, and the total volume was made up to 25 mL with water. This mixture was stirred using a magnetic stirrer at 55 °C for 30 minutes. The solution was then centrifuged and washed thoroughly, and the residue Fe_2O_3–TiO_2–CD (FeTiCD) was separated and dried. The preliminary characterization and photocatalytic efficiency studies of the FeTiCD nanocomposite were conducted using a Shimadzu 2450 double-

beam UV-visible spectrophotometer equipped with an integrating sphere accessory. Also, the band gap energy (E_g) of TiO_2, FeTi, and FeTiCD was obtained using UV-visible absorbance data using the Tauc relation[46] (see SI, Fig. S1). A Shimadzu RF6000 spectrofluorometer was used for fluorescence spectral analysis at the excitation wavelengths of 230 nm and 260 nm.

2.3. Treatment of PE nets with the photocatalytic Fe_2O_3–TiO_2–CD nanocomposite

Acid-washed high-density polyethylene (HDPE) aquaculture cage nets were dipped in a 0.02 M silane solution for 3 hours and dried at 60 °C for 3 hours in a hot-air oven.[25] Surface-modified PE netting samples (15 × 8 meshes) were immersed in various concentrations of the FeTiCD composite for 24 hours, and on the next day, they were retrieved and dried in air. This dried net sample was weighed and numbered using an aluminum token on each panel. The FeTiCD composite treatment concentrations were as follows: untreated PE (P0), silane-modified PE (P1), silane + 0.01% FeTiCD-coated PE (P2), silane + 0.02% FeTiCD-coated PE (P3), silane + 0.05% FeTiCD-coated PE (P4), and silane + 0.1% FeTiCD-coated PE (P5). Four replicates of six treatments were included in a random fashion on a PVC frame, as shown in Fig. 1, to ensure uniform exposure for each treatment. The PVC frames were submerged at a depth of 1 m from the surface during low tide at test sites at the institute in the Cochin estuary for a period of 6 months. The FTIR spectra of the composite and composite-coated net samples were obtained using a PerkinElmer Spectrum 100 spectrophotometer attached with a horizontal attenuated total reflectance (HATR) accessory. The X-ray diffraction pattern of the FeTiCD composite was analysed using a Bruker D8 advanced diffractometer with Cu Kα radiation operating at 40 kV and 35 mA. Scanning electron microscopy (SEM) images of the net panels were captured using a JEOL 6390LA at a working distance of 5 μm using an accelerating voltage of 20 kV, with magnifications ranging from 300× to 100 00×. Contact angle measurements were performed using a Rame-Hart 290-U1 contact angle goniometer.

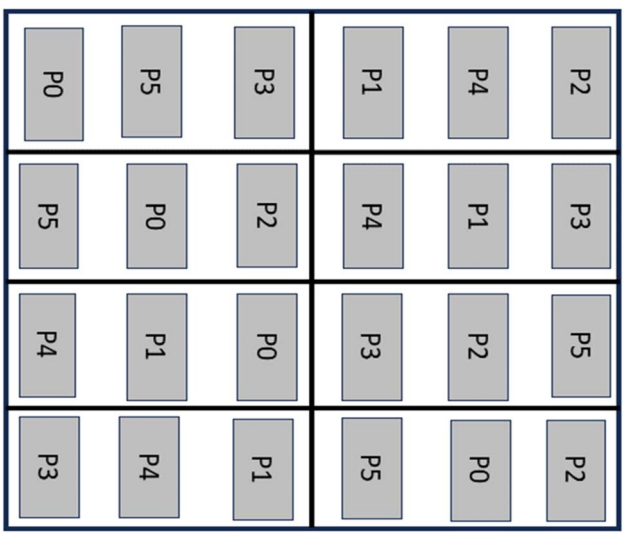

Fig. 1 Schematic of the PVC frame displaying four replicates of each treatment arranged in a random pattern.

Each frame was retrieved at the end of one month (December 2023 to January 2024), two months (December 2023 to February 2024), four months (December 2023 to April 2024) and six months (February 2024 to August 2024). The retrieved samples were washed with running water to remove adhered debris, sediments and plastic waste. Cleaned samples were dried in air after removing the token. Microscopic images of the dried net samples were taken at 25× magnification using a Leica MZ16A stereomicroscope.

3 Result and discussion

3.1. Synthesis of the FeTiCD composite

The nano-Fe_2O_3 : TiO_2 composite (FeTi) was synthesized hydrothermally, and the optimum ratio of its components was 2 : 1 (w/w basis). The FeTi–carbon dot composite (FeTiCD) was synthesized by dispersing FeTi in a nano-CD solution and heating at 55 °C for 30 minutes in a hot-air oven. The optimum ratio of FeTi : CD was 2 : 1. The composite was subjected to morphological and physicochemical characterizations and field evaluations after coating onto silane-pretreated aquaculture cage nets.

3.1.1. Spectrophotometric evaluation of the composite. UV-visible spectroscopy was performed to evaluate electronic interactions within the synthesized composite by comparing the individual spectra of each component. The individual spectra of nano-TiO_2, nano-Fe_2O_3, Fe_2O_3–TiO_2 (FeTi) and the synthesized Fe_2O_3–TiO_2–CD (FeTiCD) composite are shown in Fig. 2. CDs derived from fish skin exhibited absorption maxima at 230 and 262 nm, attributed to the π–π* transitions from the conjugated C=C carbon core and the n–π* transition from functional groups like C=O, OH, and C–N, respectively.[44] The nano-TiO_2 displayed characteristic absorption peaks at 278 and 323 nm, both within the UV region. Nano-Fe_2O_3 exhibited distinct absorption maxima at 206, 283, 370, and 501 nm. The Fe–Ti demonstrated absorption maxima at 287, 325, 450, 481 and 547 nm. The FeTiCD exhibited absorption at 217, 278, 320, 437 and 518 nm. FeTiCD exhibited prominent broader peaks in the 280–330 nm region compared with FeTi. The peak intensity ratio of 280/330 nm increased from 0.97 for FeTi to 1.01 for FeTiCD. Similarly, in the visible range, the absorption peak of FeTiCD at 437 nm became sharper and better defined compared to FeTi. The disappearance of the absorption at 481 nm for FeTiCD and a blue shift in the absorption from 547 nm (FeTi) to 518 nm (FeTiCD) with a lower intensity were observed. The successful integration of CDs into FeTi was evidenced in FeTiCD by the presence of peaks at 217 and 278 nm. The broader absorption at 278 nm had a higher intensity ratio (217/278 nm), which was contributed by TiO_2 and the functional groups responsible for the n–π* transition. The extended absorption into the visible range suggests that the composite can effectively utilize sunlight, overcoming the inherent UV-region limitation of pristine TiO_2.[47,48]

The band gap was calculated based on Tauc's equation. For bulk anatase TiO_2, the band gap is typically around 3.2 eV.

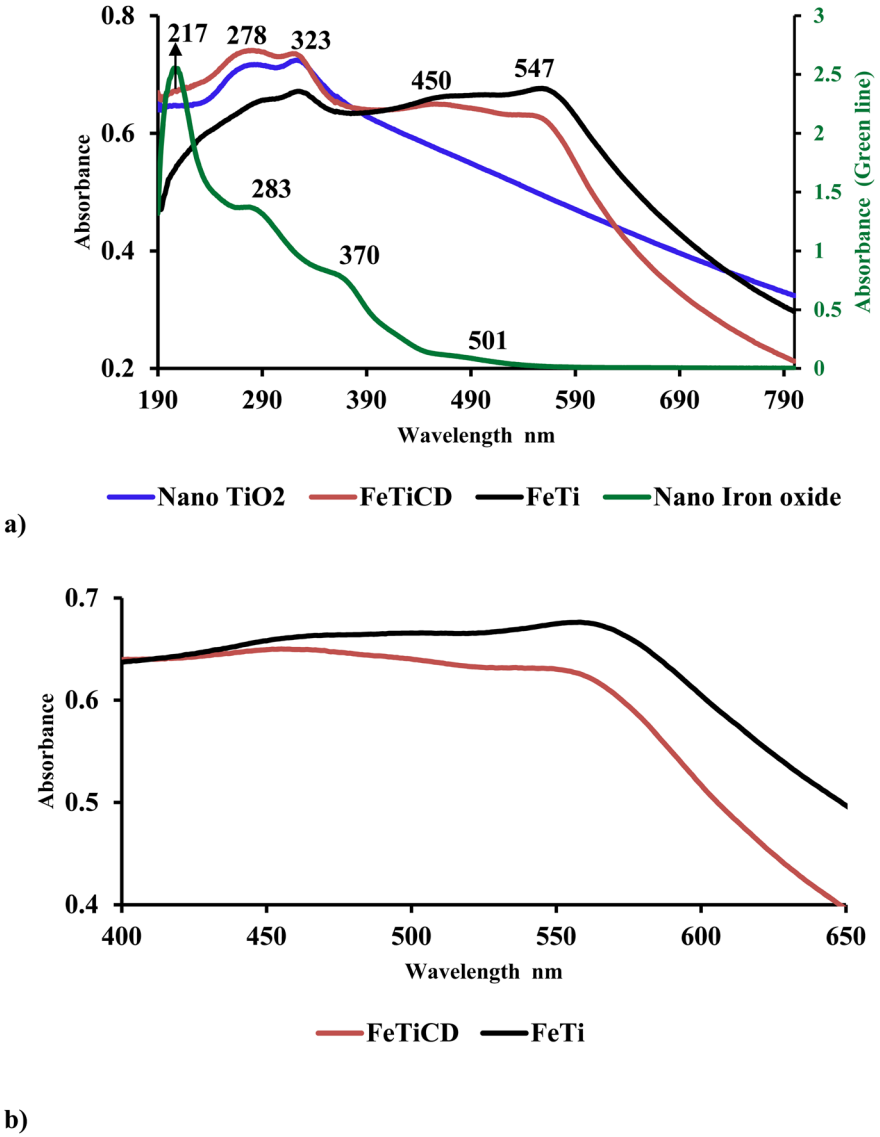

Fig. 2 UV-visible spectra of (a) nano-iron oxide, nano-TiO_2, FeTiCD and FeTi (nano-iron oxide (green line) is shown in the secondary axis) and (b) FeTiCD and FeTi in the visible range (400–600 nm).

Quantum confinement effects can cause the band gap of TiO_2 to increase, if it is in nanoscale range. The observed increase in the band gap can be attributed to the reduction in the crystallite size compared to the bulk material. As the crystallite size decreases, electrons become spatially confined within a smaller region, leading to an expansion of the energy separation between the valence band (VB) and conduction band (CB). Consequently, a higher energy input is required for electrons to transition from the VB to CB. This phenomenon is well explained by the quantum confinement effect (QCE), which states that the band gap energy increases with decreasing crystallite size, and *vice versa*.[49,50] In bulk semiconductors, electrons and holes occupy continuous allowed and forbidden energy bands. When the material dimensions approach the nanoscale, quantum confinement results in discrete, size-dependent energy levels rather than continuous bands. Therefore, the VB and CB edges shift relative to those of the bulk counterpart, thereby widening the band gap energy.[51] Results showed that the incorporation of Fe^{3+} and CDs into TiO_2 introduced an intermediate energy level below the conduction band, narrowing the band gap from 4 eV (TiO_2) to 2 eV in FeTi and further to 1.7 eV in FeTiCD. This modification enabled the visible light absorption of the composite (detailed description is given in SI, Fig. S1(a–c)). CDs exhibited fluorescence with the highest emission maxima at 445 nm at an excitation wavelength of 220 nm.[38] The fluorescence of CDs was quenched in the FeTiCD composite upon the incorporation of CDs into FeTi (SI, Fig. S2). The introduction of CDs into the metal oxide matrix altered the bandgap, inducing charge separation and delayed e^-/h^+ recombination, leading to fluorescence quenching.[52] The results clearly establish that CDs interact with metal oxides through conjugated C=C bonds and other functional groups to

form FeTiCD. The composite is expected to exhibit increased photocatalytic properties and delayed e^-/h^+ recombination.

Narrowing the band gap of TiO_2 is expected to decrease the reducing and oxidizing power, respectively, due to the less negative valence band maximum and less positive conduction band maximum.[53,54] The introduction of iron oxide and carbon dots in the FeTiCD composite reduced the bandgap and significantly increased the visible light absorption, leading to enhanced population of e^-/h^+ pairs and hence increased photocatalytic reactions. Carbon dot improved the photocatalytic activity of iron oxide, while formation of the FeTiCD composite through coupling with TiO_2 decreased the bandgap of TiO_2 in the composite.[55,56]

3.1.2. Evaluation of the photocatalytic efficacy. The photodegradation of methylene blue (MB) using FeTiCD was studied in MilliQ water, 3.5% NaCl, and seawater for 5 hours under sunlight. The water with methylene blue, methylene blue + FeTiCD and photodegraded methylene blue after 5 h exposure to light is shown in Fig. 3(a–c). FeTiCD exhibited an orange colour in water and seawater, whereas in 3.5% NaCl, it exhibited

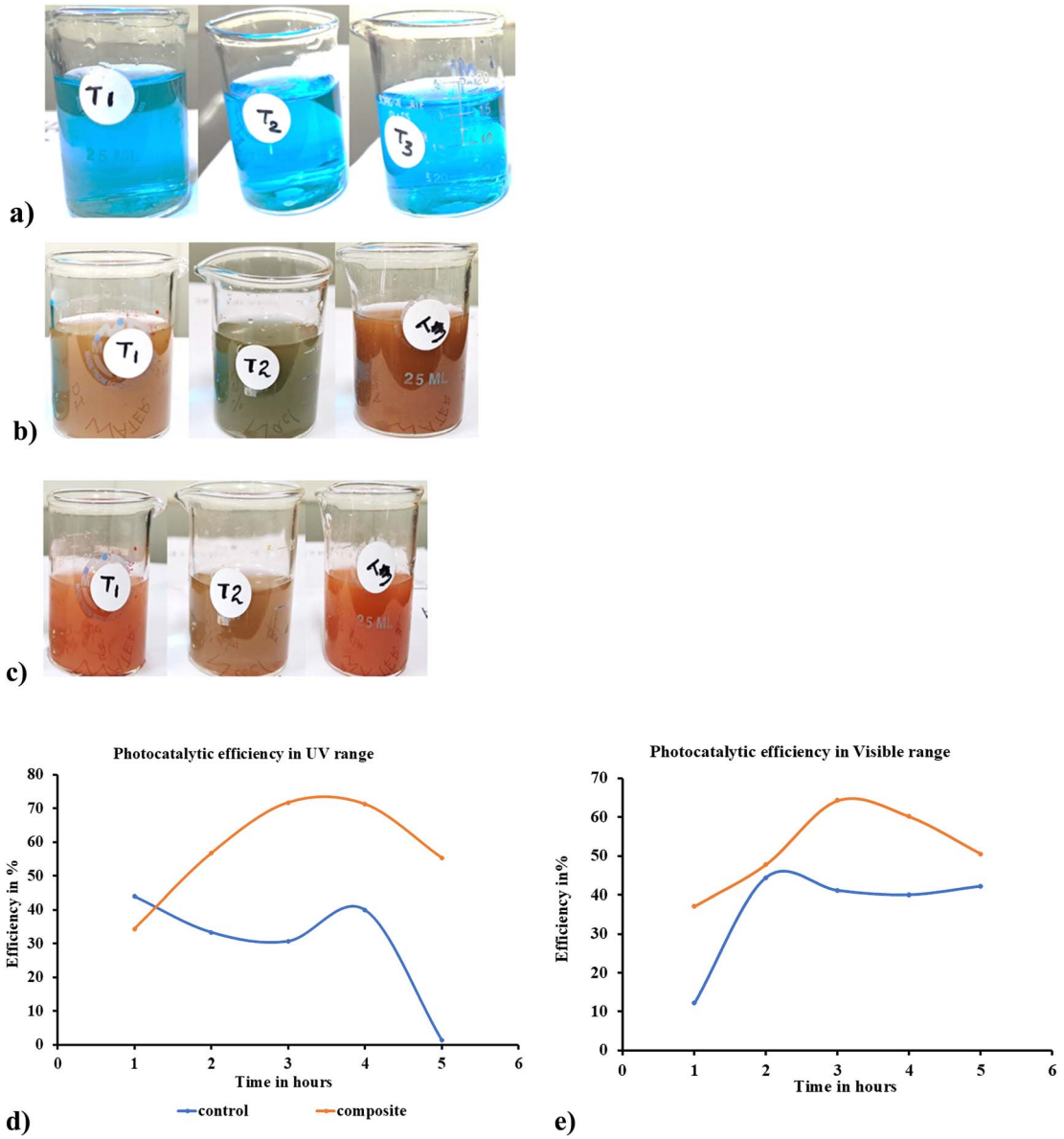

Fig. 3 (a–c) Photodegradation of methylene blue dye. (a) Methylene blue in different aqueous environments, namely, distilled water (T1), 3.5% NaCl (T2), and seawater (T3), without the composite before exposure to sunlight. (b) Methylene blue dye + FeTiCD in distilled water (T1), 3.5% NaCl (T2), and seawater (T3) before exposure to sunlight. (c) Methylene blue dye + FeTiCD after exposure to sunlight for 5 hours. (d) Photocatalytic efficiency of FeTiCD in the UV range. (e) Photocatalytic efficiency of FeTiCD in the visible range.

a greenish-orange colour. The greenish-orange colour exhibited in 3.5% NaCl was probably due to the increased ionic strength of NaCl due to the Na^+ and Cl^- ions, and their interaction with the oxides of FeTiCD might have shifted the absorption towards the blue region. After exposure to sunlight for 5 h, the beakers containing water and seawater exhibited an intense orange colour and a faded orange colour was observed in 3.5% NaCl. The results clearly showed that the methylene blue dye was degraded, and the color of the composite reappeared. The FeTiCD was efficient enough to degrade the MB dye in different aquatic environments. Here, Fe^{3+} probably served as an oxidizing agent, capturing electrons on the TiO_2 surface, thereby promoting charge separation and reducing recombination.[57,58] The incorporation of Fe^{3+} and CDs into TiO_2 introduced intermediate energy levels below the conduction band of TiO_2 and led to the generation of hydroxyl radicals, which effectively oxidized MB into smaller molecules.[4] The ability of the composite to generate ROS ensures its application as a potential material for antifouling applications.

The UV-visible spectroscopy of FeTiCD + dye in seawater was performed at hourly intervals to monitor the changes in the absorbance of the seawater samples exposed to sunlight with and without the MB dye. The absorbance intensities at 290 nm (UV region) and 665 nm (visible region) were recorded for both control (MB in water) and MB + FeTiCD-treated solutions. The photocatalytic efficiency was then calculated based on the variation in the absorbance intensity. Fig. 3(d) presents the photocatalytic efficiency under UV irradiation, where the synthesized photocatalyst showed enhanced performance compared to the control. Initially, the photocatalyst exhibited adsorption or partial degradation of the dye, followed by a significant increase in activity, which eventually stabilized, whereas the control displayed fluctuations and a considerable decrease in efficacy. This indicates the efficient utilization of UV light for the generation of reactive species and effective photocatalytic degradation.

Fig. 3(e) shows the photocatalytic efficiency under visible light, where the photocatalyst consistently outperformed the control throughout the experiment. Initially, the photocatalyst demonstrated efficient absorption of visible light and higher degradation rates compared to the control. Although a slight decline in activity was observed at later stages, possibly due to reduced availability of active sites, the photocatalyst maintained superior performance. The enhanced activity of the synthesized photocatalyst can be attributed to the efficient separation of e^-/h^+ pairs, as well as modifications and interactions among the composite components, which resulted in an improved surface area, thus leading to enhanced light harvesting and increased photocatalytic efficiency.[59,60] The degradation of the MB dye by the composite established the composite's photocatalytic characteristics.

3.1.3. FTIR analysis of the composite. The FTIR spectral data of FeTi and FeTiCD are presented in Fig. 4 and SI, Table S1. The broad Fe–O bond stretching vibration was initially observed at 518 cm^{-1}, which shifted to 511 cm^{-1} after the incorporation of CDs, resulting in a sharp peak, confirming the enhanced structural order.

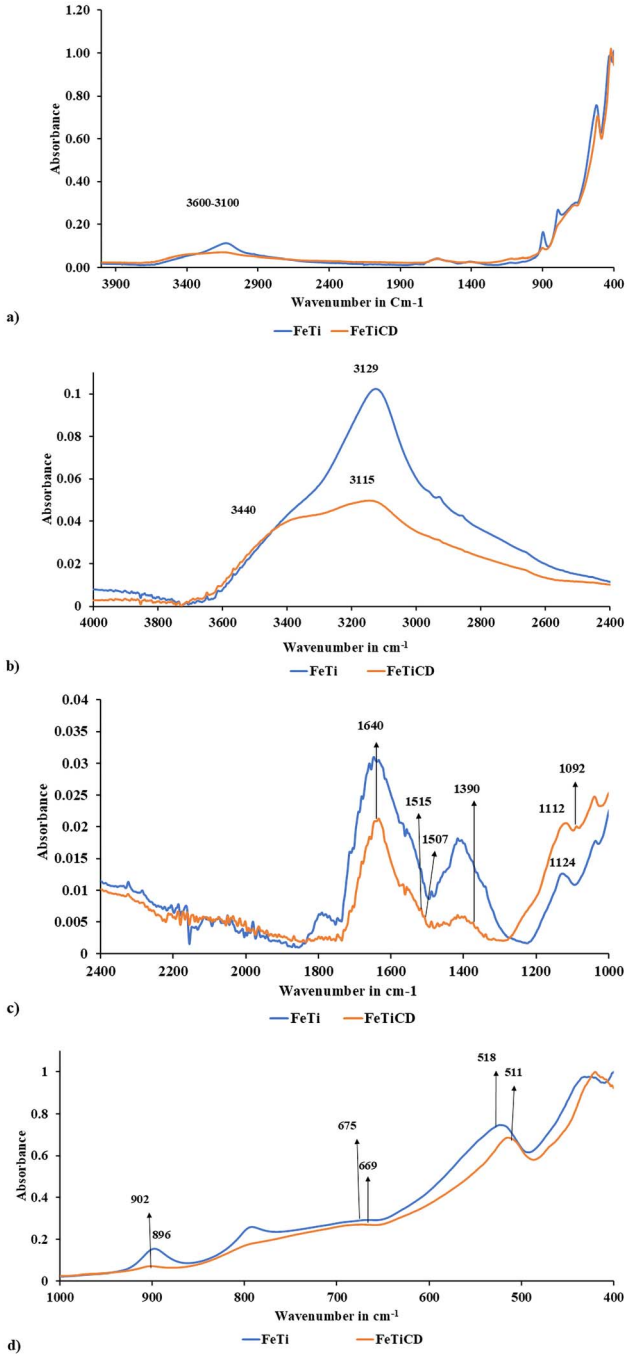

Fig. 4 FTIR absorption spectra of (a) FeTi and FeTiCD composite recorded in the range of 400–4000 cm^{-1} using μATR FTIR. The spectral graphs were shown expanded from (b) 4000 to 2400 cm^{-1}, (c) 2400 to 1000 cm^{-1} and (d) 1000 to 400 cm^{-1}, for better understanding of absorption peaks of sample.

The Ti–O bond peaks at 669 and 896 cm^{-1} in FeTi and FeTiCD shifted to 675 and 902 cm^{-1}, respectively, and the latter peak was wider and more suppressed. This clearly showed that the CDs interacted with the oxygen atom of the FeTi composite. The absorption corresponding to the O–H bond stretching of phenols/tertiary alcohol of CDs at 1390 cm^{-1} became more defined in FeTiCD, indicating the strong coordination bond-

type interaction of O–H with metal oxides, and this was evidence by the wider absorption around 3600 cm^{-1}. The aromatic C=C–C stretching vibration of fish skin-derived CDs was observed at 1454 and 1515 cm^{-1},[44] and the absorptions in FeTiCD at 1507 and 1515 cm^{-1} indicated the interaction of aromatic C=C with metal oxide bonds. The triplet at ~1640 cm^{-1}, related to Fe–O and Ti–O bond bending vibrations, changed to a doublet upon the modification of the metal oxide composite with CDs. A shift in the aromatic C–H stretching frequency of CDs was observed from 3125 to 3115 cm^{-1} after FeTiCD formation. The peaks corresponding to C–H stretching vibrations of CH_2 and CH_3 groups introduced by CDs were observed as nicks and were masked by the dominating metal oxide absorptions around 3000 cm^{-1}. The hydrogen bonded OH stretching vibration of metal oxides with CD exhibited wider absorption peak spanning from 3100 to 3600 cm^{-1} in FeTiCD composite. The conjugated C=C system of CDs and OH groups mainly interacted with the Ti–O and Fe–O bonds in the composite through van der Waals, coordination-type or hydrogen bonding interactions, which led to the successful formation of the composite.

3.1.4. Transmission electron microscopy (TEM) of the FeTiCD composite. TEM was carried out to verify the nanoscale distribution of the FeTiCD composite, as given in Fig. 5(a and b). The micrographs revealed a uniform distribution of nano-scale domains, with no evidence of particle agglomeration or the formation of isolated clusters. The micrographs exhibited well-resolved lattice lines with an interplanar spacing of ~0.26 nm, indicating the crystalline nanophases of TiO_2 and Fe_2O_3. The diffused region in the micrographs highlighted the presence of amorphous CDs and their distribution around Ti and Fe oxides. This homogeneous distribution stands in clear contrast to the microstructural characteristics typically associated with simple mechanical mixing, which generally results in the formation of irregular aggregates or distinct phase-separated regions.

3.1.5. X-ray diffraction (XRD) analysis of the FeTiCD composite. The XRD pattern of the FeTiCD composite is shown in Fig. 6. The phase identification of anatase TiO_2 was done by comparing experimental data with the standard peak positions obtained from NIST's POWD-12++ database, as originally reported by Cromer and Herrington.[61] FeTiCD exhibited prominent peaks at $2\theta = 25.3°$, 48.0°, 55.1°, 62.1°, and 68.7°, indexed to (101), (200), (211), (213), and (116), respectively. Additional peaks observed at $2\theta = 24.2°$, 33.2°, 35.7°, 40.9°, 49.6°, 54.2°, 57.6°, and 62.6° were indexed to (012), (104), (110), (113), (204), (116), (122), and (214), respectively. These peaks corresponded to the hematite, Fe_2O_3, according to the XRD data obtained from ICSD using POWD-12++, as reported by Yu *et al.*[62,63] The XRD pattern of anatase TiO_2 exhibited peaks at ~37° and ~75°, corresponding to high index planes,[61] whereas the XRD pattern of the hematite (iron oxide) showed a peak at ~75°.[62,63] In the FeTiCD composite, the peaks were observed at ~37° and ~75° with high indexed planes, such as (004) and (215), respectively; this confirmed the presence of nano-TiO_2 and nano-Fe_2O_3 in the composite matrix. Experimental XRD data confirmed the successful incorporation of Fe_2O_3 and TiO_2 into the composite. The sharp peaks of TiO_2 and Fe_2O_3 suggested nano-scale crystallinity. High-index planes, such as (213), (116), (204), and (104), which often appear as weaker diffraction peaks, suggested small crystallite size, lattice strain, or the presence of nanostructuring.[64] The broad and weak peak centered at $2\theta = 21°$ suggested the presence of amorphous or low-crystallinity CDs with a graphitic core. This peak usually corresponds to sp^2 hybridized carbon. A minor shift in the peak position indicated the lattice interaction between these oxides, possibly due to interfacial strain or partial substitution.[65] The XRD analysis confirmed the successful formation of the composite,

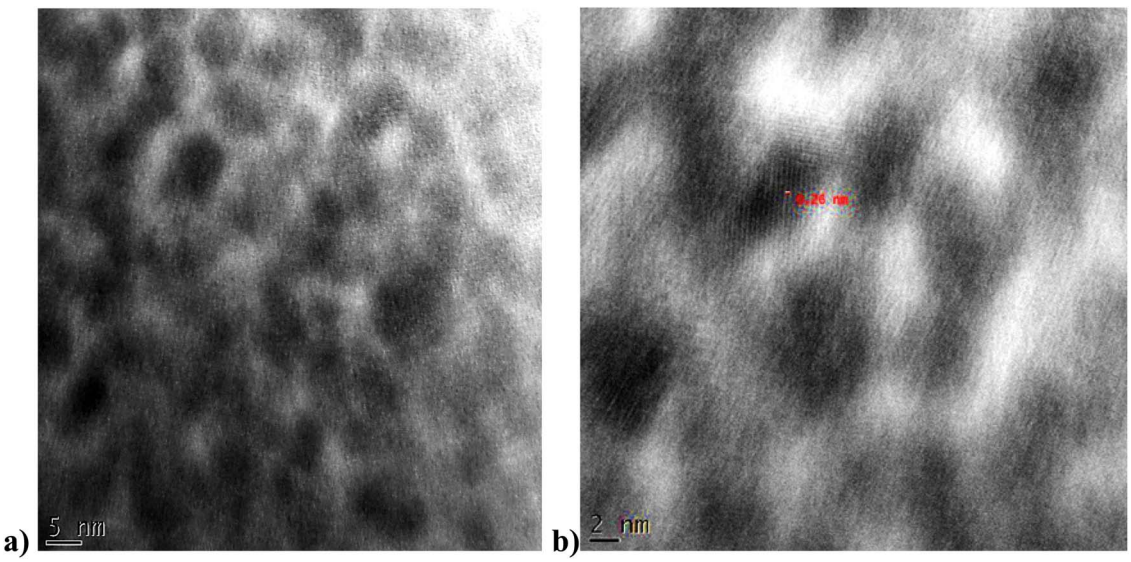

Fig. 5 (a) Low-magnification TEM image (scale bar: 5 nm) illustrating the homogeneous distribution of nano-sized features in the FeTiCD composite. (b) HRTEM image (scale bar: 2 nm) displaying clear lattice fringes, confirming the crystalline nature of the Fe–Ti phases and their effective integration with carbon dots.

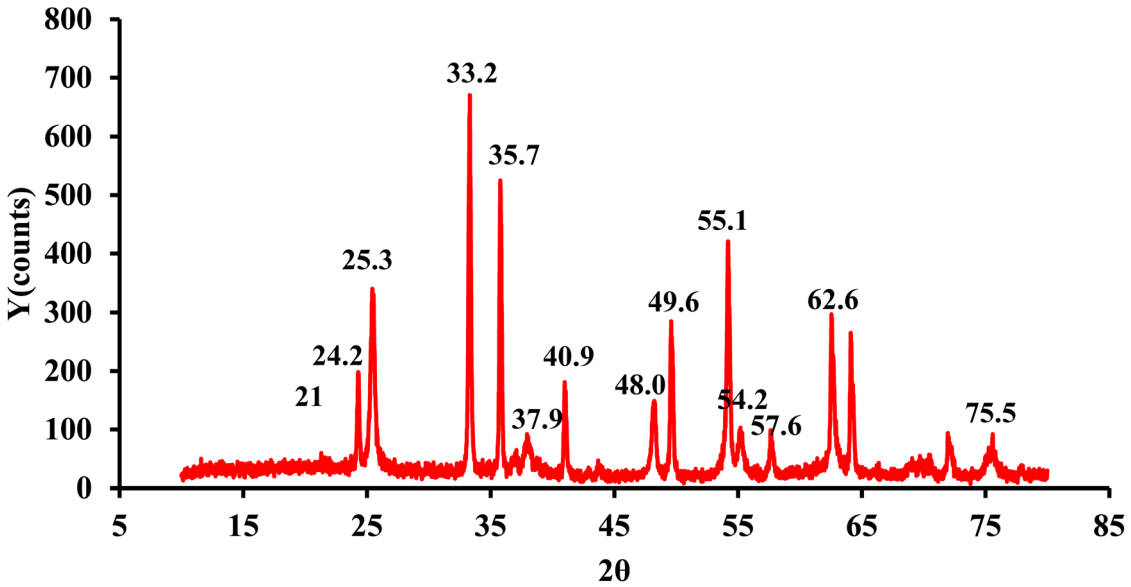

Fig. 6 X-ray diffractogram of the FeTiCD composite using powder XRD.

as evidenced by the characteristic diffraction peaks corresponding to TiO_2, Fe_2O_3, and CDs, which are in good agreement with the standard reference patterns. These results validated the successful integration of the individual components and highlighted the potential of the synthesized material for application as a photocatalytic nanocomposite.

3.2. FeTiCD composite-coated HDPE cage nets

Silane-pretreated polyethylene aquaculture cage nets were immersed overnight in varied concentrations of FeTiCD solutions (0.01% to 0.10%), and the retrieved nets were characterized and exposed to an estuarine environment to study the biofouling resistance of aquaculture cage nets after the biocide treatment.

3.2.1. Surface morphology

3.2.1.1. Scanning electron microscopy (SEM). Scanning electron microscopy with energy-dispersive X-ray analysis (SEM-EDAX) was employed to analyze the surface morphology and elemental composition of the synthesized material. The surface of PE (Fig. 7(a)) exhibited noticeable unevenness and roughness. However, after silane treatment (Fig. 7(b)), no particulate or crystalline structure was observed, implying the uniform coating of silane over PE. Coating FeTiCD over the silane-treated polyethylene (Fig. 7(c)) resulted in a more granular and particulate morphology and homogenously distributed FeTiCD on the surface. The presence of FeTiCD in the matrix may influence antimicrobial properties, potentially due to its previously established increased activity under visible light. The quantitative elemental composition of silane-pretreated HDPE nets was determined by SEM-EDX analysis, as given in Fig. 7(d), and the weight percentages (wt%) of C, Si, and O, respectively, were 84.08, 0.34 and 15.58 wt%. This clearly established the formation of the silane coating over the polyethylene net. In contrast, the FeTiCD-coated silane-pretreated HDPE net showed a dominant carbon peak at 0.27 keV (100%), along with a weak Si signal at 1.74 keV, as given in Fig. 7(e). The Fe and Ti peaks were expected between 6 and 7 keV but only appeared as weak signals, probably due to the nanoscale concentration of Fe and Ti, which was below the detection limit and further obscured by the strong carbon absorption originating from the polyethylene substrate and carbon dots. Such situations are expected when analytes are present in either very high or very low concentrations within the material. The results indicated that the FeTiCD is strongly embedded on the silane-coated PE surface, and its FTIR characteristics will determine the nature of the interaction of the biocide with silane.

3.2.2. FTIR analysis of FeTiCD-coated silane-pretreated HDPE. Fourier transform infrared (FTIR) spectroscopy was employed to characterize the FeTiCD-coated aquaculture cage nets (Fig. 8 and Table S2) and the interaction between various materials on the silane-coated surface. FTIR analysis provided strong evidence of interactions between the FeTiCD composite and the silane-modified PE matrix. The triplet C–O–C symmetric stretching absorption in PE-silane and silane + FeTiCD coated nets shifted from around 825 to 803 cm^{-1}, respectively, suggested an interaction between the epoxy bond of the organosilane and the composite. Similarly, the asymmetric C–O–C stretching frequency shifted of silane-PE surface from 1251 to 1242 cm^{-1}, further indicated possible coordination effects or electron donation interactions between the composite and the silane matrix. The Si–O–C stretching frequencies, originally observed at 1139 and 1200 cm^{-1} in silane-coated PE, shifted to 1145 and 1210 cm^{-1}, respectively, upon coating with the FeTiCD composite. This shift towards higher wavenumbers suggested an increase in bond strain[66] and confirmed the formation of a hybrid organic–inorganic system between the composite and the silane-functionalized PE. Furthermore, the emergence of new absorption bands at 1532, 1567, 1629 and 1645 cm^{-1}, corresponding to C=C aromatic stretching, C=C conjugation, and C=C aryl vibrations,

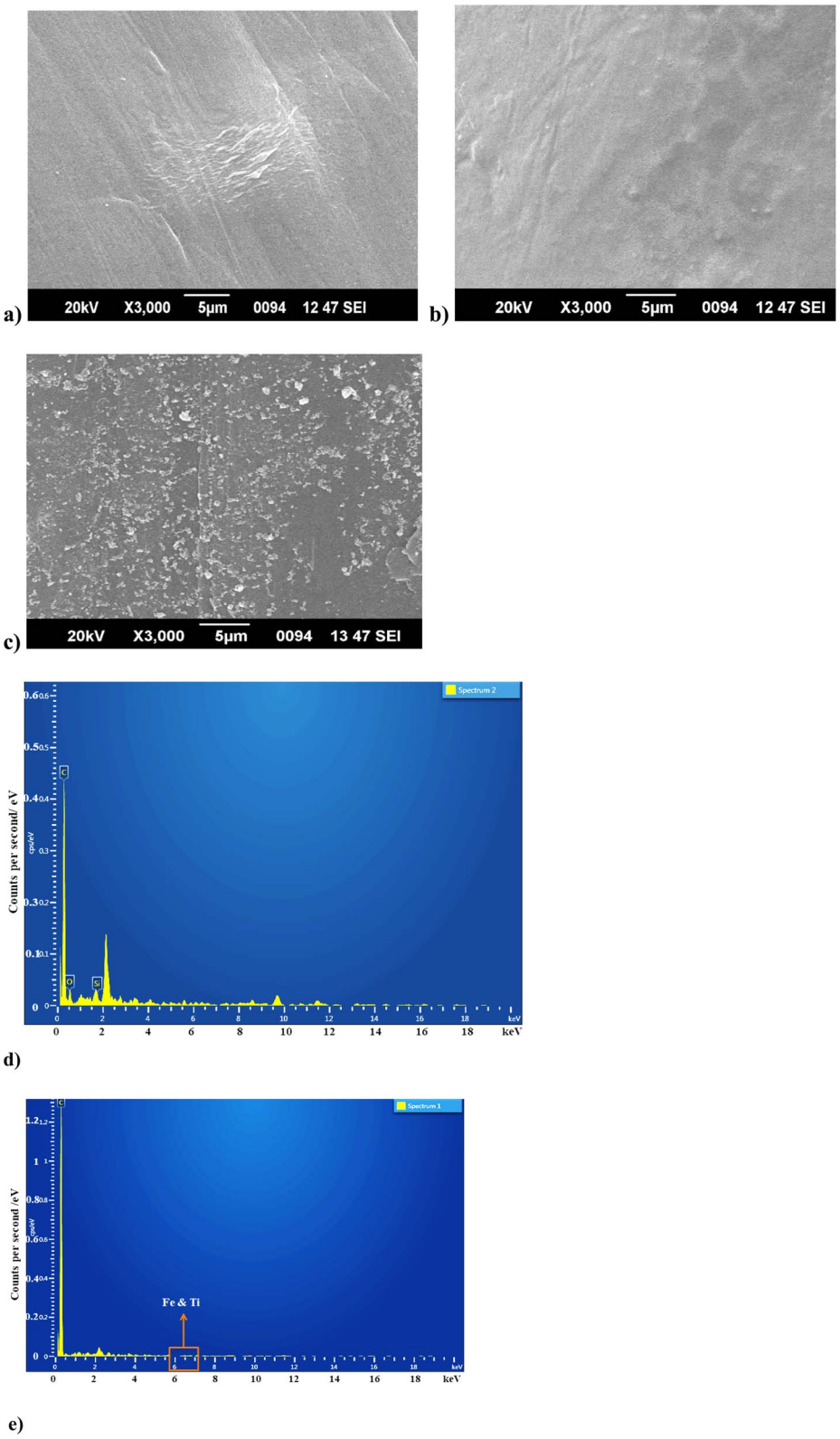

Fig. 7 Scanning electron micrographs of (a) untreated polyethylene, (b) silane-treated polyethylene, and (c) FeTiCD-coated silane-pretreated polyethylene, depicting the uniform silane coating and homogeneous FeTiCD distribution on PE cage nets, recorded at 3000× magnification with a 5 µm scale bar. The EDAX spectra of (d) silane-treated polyethylene and (e) FeTiCD-coated silane-pretreated polyethylene aquaculture cage nets plotted with the X-ray energy (keV) on the *X*-axis and X-ray intensity counts on the *Y*-axis.

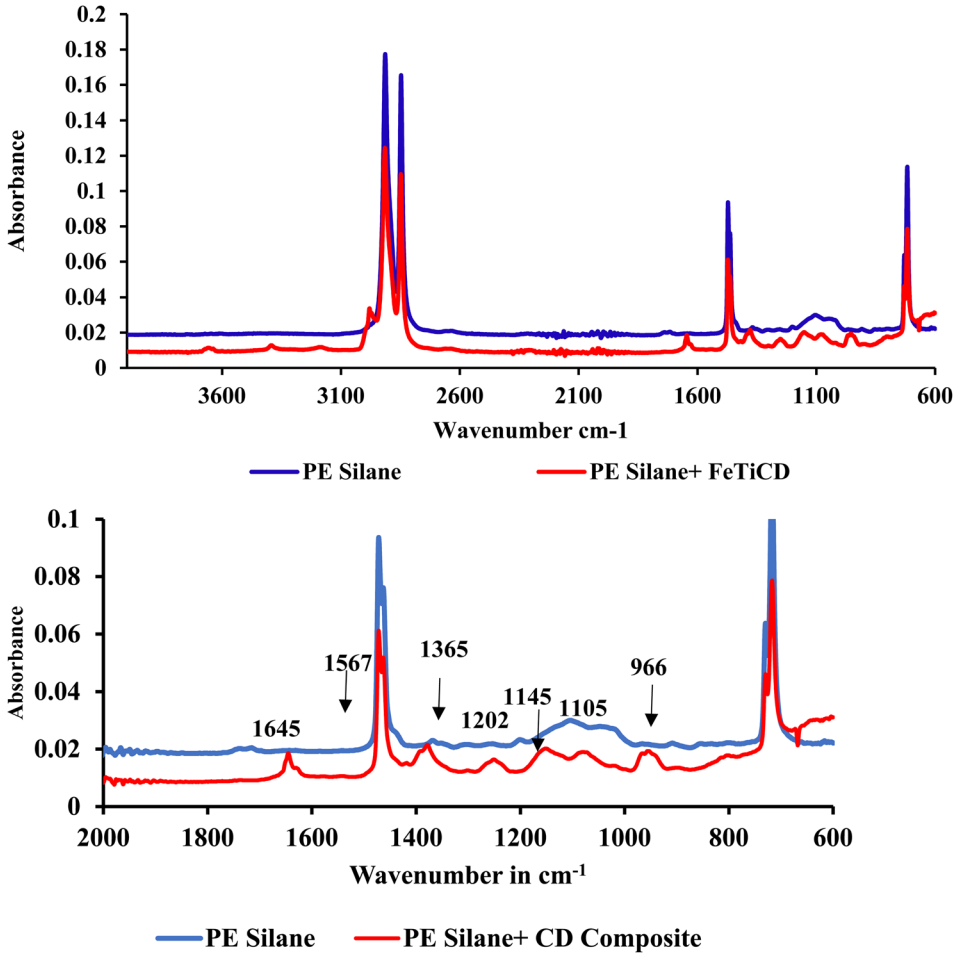

Fig. 8 FTIR spectra of silane-pretreated and FeTiCD-coated silane-pretreated polyethylene aquaculture cage nets.

respectively, provided clear evidence of the successful incorporation of CDs into the composite matrix. The additional peaks at 3633 cm^{-1} and 3651 cm^{-1}, associated with hydroxyl (–OH) functional groups from CDs, indicated potential hydrogen bonding and π–π interactions between CDs and the silane-treated PE matrix. These spectral modifications confirmed that the FeTiCD composite was effectively integrated into the PE-silane network through epoxy bonds, π–π interactions and hydrogen bonding, leading to enhanced structural interactions that contributed to the stability and functional properties of the composite.

3.2.3. Hydrophobicity and surface interaction analyses of coated polyethylene films. The surface wettability of the FeTiCD-coated aquaculture cage net was evaluated by contact angle measurements using a contact angle goniometer (Fig. 9). A 10 μL drop of seawater was gently deposited on the FeTiCD-coated surface of a silane-pretreated polyethylene sheet, and the contact angle was determined using the static method. For each sample, measurements were repeated at 10 different positions to ensure uniformity. The silane-pretreated polyethylene surface exhibited a contact angle of 94.12° ± 1.78°, and FeTiCD-coated silane-treated PE exhibited an angle of 94.45° ± 0.052°. The difference in the surface wettability of silane-treated PE and FeTiCD-coated silane-treated PE was evident from the contact angle measurement. The photocatalytic FeTiCD composite coated over silane-treated PE slightly enhanced the hydrophilic nature. This suggests that the composite lowers the surface energy due to increased surface roughness or may be due to the presence of low-surface-energy functional groups. The improved wettability will deter organic and proteinaceous material attachment over the surface, leading to deterred microorganism attachment, slow biofilm formation and hence biofouling inhibition.

3.2.4. Field exposure studies. As described in the Materials and methods (Section 2.3), different concentrations of FeTiCD were coated over the polyethylene aquaculture cage net surface modified with silane, and the treatments were designated as P0–P5. The preweighed and tagged treated net samples were exposed to an estuarine environment for six months. The samples were retrieved at the end of one (December 2023 to January 2024), two (December 2023 to February 2024), four (December 2023 to April 2024), and six (February 2024 to August 2024) months. For each retrieval, the biomass accumulated per gram of the net was recorded and is presented in Fig. 10. During the six-month period of exposure to the estuarine environment, the treated nets P4 (0.05% composite) and P3 (0.02% composite) exhibited the lowest biomass accumulation, except in the second month. In the second month, all the panels were

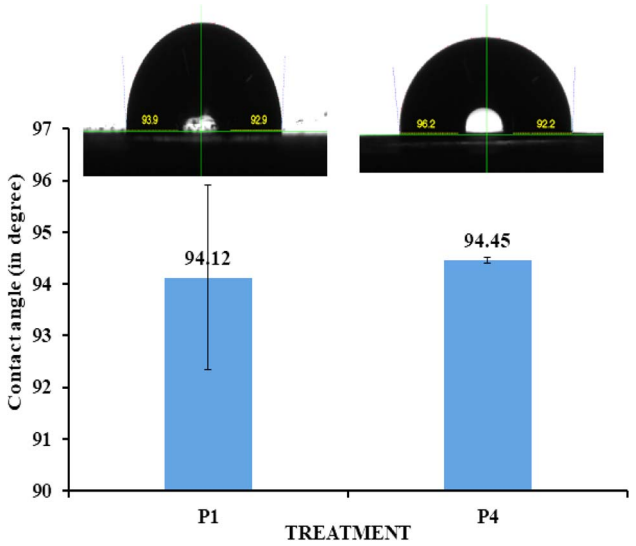

Fig. 9 Representative contact angle images obtained *via* the static drop method using seawater on the surface of silane-pretreated polyethylene (P1) and FeTiCD-coated silane-pretreated polyethylene (P4). Plots showing the average contact angles measured for the silane-pretreated polyethylene (PE) and FeTiCD-coated silane-pretreated PE surfaces.

infected with *Mytella strigata* spats, an alien marine species potentially introduced *via* ballast water in the Cochin Port region,[67] and hence, the results were not comparable. In the fourth and sixth months, P4 exhibited the lowest biomass accumulation compared to the untreated control. Among P3 and P4, the latter had a higher concentration of FeTiCD but both exhibited almost similar performance. Hence, P4 (0.05% FeTiCD) was taken as the optimum for the best performance. Increasing the concentration of FeTiCD on the net did not lead to improved antifouling properties. This may be due to factors such as the formation of multiple composite layers, increased molecular aggregation, unfavourable interactions with seawater, and changes in the microbial community structure, which will lead to a thicker biofilm and reduced antifouling efficiency due to saturation.[68,69] Biofouling inhibition in the aquaculture cage net was explained mainly based on the efficient generation of ROS, which deterred the micro and macro-organisms in the vicinity of the net.

The salinity in the estuary during 1, 2, 4 and 6 months, respectively, was 19.77, 28.39, 29.81 and 12.8 psu. Similarly, the pH levels in 1, 2, 4, and 6 months, respectively, were 7.93, 7.59, 7.99 and 7.02. The dissolved oxygen levels in 1, 2, 4 and 6 months, respectively, were 1.6, 2.4, 2.0, and 2.4 mg L^{-1}. The elevated salinity in the 4th month might have contributed to the higher biomass accumulation in the treated cage nets, as higher salinity accelerates biofouling development.[70] The fourth-month retrieval coincided with the premonsoon season, during which the fouling intensity was high. In contrast, during the sixth-month retrieval, which occurred during the monsoon season, the low pH and salinity and high DO levels supported the growth of hydroids, which became the dominant fouling organisms attached to the net surfaces during this period. The results clearly established that the 0.05% FeTiCD-coated silane-pretreated polyethylene surface has the highest biofouling inhibition.

3.2.5. Mechanism of photocatalytic activity in the Fe_2O_3–TiO_2–carbon dot nanocomposite for antifouling applications. TiO_2 efficiently generates e^-/h^+ pairs under UV irradiation due to its wide bandgap (4 eV), which limits its photocatalytic activity under visible light. Surface modification strategies, including metal doping and nano-carbon dot incorporation, have been explored to enhance its visible light response.

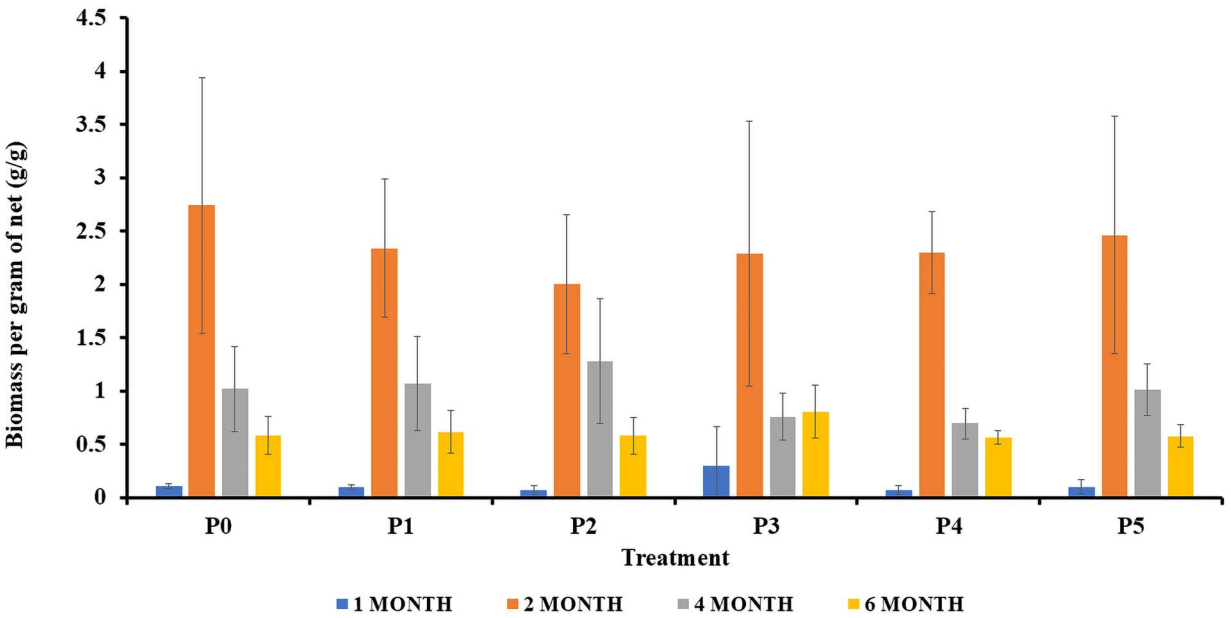

Fig. 10 Biomass accumulation (g g^{-1} of net) on nets exposed to the estuarine environment for 6 months.

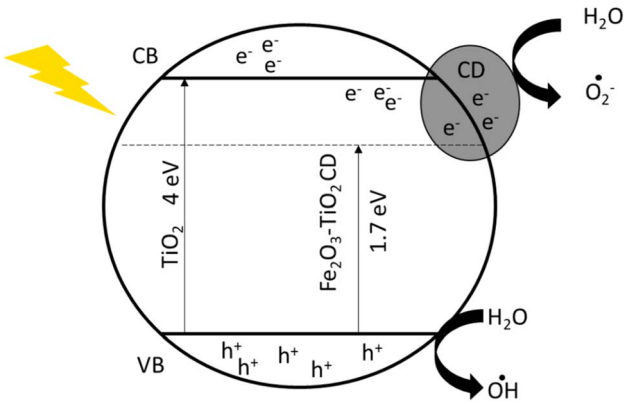

Fig. 11 Schematic of the reduced band gap of the FeTiCD composite and the mechanism of ROS generation.

However, studies involving the simultaneous incorporation of metal ions and nano-carbon analogues into TiO_2 remain limited.

In this study, TiO_2's surface is modified with nano-Fe_2O_3 and CDs. The incorporation of Fe(III) introduces mid-gap states between the valence and conduction bands, effectively reducing the bandgap of the composite. This shift is confirmed by the observed redshift in the absorption spectrum, indicating enhanced absorption in the visible region. Consequently, the composite can harness visible light photons to generate ROS. Fe(III) ions act as electron acceptors, suppressing e^-/h^+ recombination and prolonging charge carrier lifetimes.[71]

The narrowing of the bandgap can also be attributed to Ti–O–C bonding, which facilitates efficient charge transfer.[72] According to John and Achari,[3] in the presence of graphene, photogenerated electrons transfer from the conduction band (CB) of TiO_2 (d-orbital) to the Fermi level of graphene (π-orbital), enhancing charge separation and further promoting ROS generation.[3]

The proposed mechanism for the enhanced photocatalytic activity of the composite is provided in Fig. 11. Fe(III) doping introduces a new energy level within the TiO_2 bandgap, allowing photogenerated electrons to transfer to the modified conduction band, while holes remain in the valence band. The electrons in the conduction band are further accepted by CDs, which facilitate their transport to the surface, where they interact with water and oxygen to generate ROS, including superoxide ($O_2^{\bullet-}$), hydroperoxyl ($HO_2^{\bullet}$), and hydroxyl radicals ($^{\bullet}OH$). The reduced recombination rate ensures continuous ROS generation, effectively counteracting fouling agents. This study demonstrates that the synergistic effects of Fe(III) and CD incorporation significantly enhance the photocatalyst-mediated antifouling properties of TiO_2, making it a promising material for environmental applications.

4 Conclusion

A photocatalytic iron oxide–titanium dioxide–carbon dot nanocomposite was synthesized; and results revealed that FeTiCD was successfully formed, and FeTi interacted with conjugated C=C bonds of CDs, resulting in a reduced bandgap. FTIR spectra confirmed that the conjugated C=C bonds in CD interacted with oxygen moieties of the Fe–O and Ti–O bonds, most likely *via* hydrogen bonding, coordination, or van der Waals interactions involving the amine and hydroxyl groups introduced by CD into the matrix. It expanded visible-light absorption by reducing the bandgap to 1.7 eV, and iron oxide's and CDs' interaction with TiO_2 enhanced photocatalytic efficiency by delaying e^-/h^+ recombination, resulting in the generation of ROS. The FeTiCD composite was coated onto silane-pretreated polyethylene cage nets, exhibiting strong adhesion *via* C–O–C bonds, π–π interactions, and hydrogen bonding, forming a stable organic–inorganic system between organosilane and the composite. The 0.05% composite-coated nets demonstrated superior antifouling performance after six months of exposure, making them a promising antifouling material. The present study emphasized the use of organosilane compounds as surface modifiers of nonpolar polyethylene and their effectiveness in holding biocides to deter the biofoulers in the aquatic environment. The contamination of the environment due to the nanomaterial is of little concern because the net is immersed in a 0.05% composite solution, making its impact very limited.

Author contributions

P. M. Ashraf: conceptualization and planning, writing the manuscript and data interpretation. Gopika R.: synthesis and application of the composite, laboratory experiments, data compilation, and manuscript writing.

Conflicts of interest

The authors declare no conflicts of interest.

Data availability

The data supporting this research paper are available from the corresponding author and will be shared upon reasonable request.

Supplementary information (SI): the application of Tauc equation (Fig S1), fluorescence spectra of FeTiCD composite (Fig S2), detailed FTIR absorption frequencies of FeTi and FeTiCD composite (Table S1) and spectral data of silane pretreated and FeTiCD coated silane pretreated polyethylene aquaculture cage net (Table S2). See DOI: https://doi.org/10.1039/d5ra09273f.

Acknowledgements

DST INSPIRE India provided financial support to the research scholar in the form of a scholarship and contingencies. The authors sincerely thank the Director, ICAR-Central Institute of Fisheries Technology and the Head of Fishing Technology and Microbiology Fermentation and Biotechnology Division for providing facilities. Gratitude is also extended towards the Sophisticated Technology Instrumentation Centre, Cochin, for

providing SEM facilities for samples analysis. The DST-INSPIRE programme is acknowledged for providing financial support.

References

1 R. Ameta, M. S. Solanki, S. Benjamin and S. C. Ameta, in *Advanced Oxidation Processes for Waste Water Treatment*, Academic Press, 2018, pp. 135–175, DOI: 10.1016/B978-0-12-810499-6.00006-1.
2 R. Ullah and J. Dutta, *J. Hazard. Mater.*, 2008, **156**, 194–200, DOI: 10.1016/j.jhazmat.2007.12.033.
3 D. John and V. S. Achari, *Curr. Sci.*, 2022, **123**, 1089–1100, DOI: 10.18520/cs/v123/i9/1089-1100.
4 D. I. Anwar and D. Mulyadi, *Procedia Chem.*, 2015, **17**, 49–54, DOI: 10.1016/j.proche.2015.12.131.
5 Z. Zhan, H. Wang, Q. Huang, S. Li, X. Yi, Q. Tang, J. Wang and B. Tan, *Small*, 2022, **18**, 2105083, DOI: 10.1002/smll.202105083.
6 T. S. Natarajan, J. Y. Lee, H. C. Bajaj, W. K. Jo and R. J. Tayade, *Catal. Today*, 2017, **282**, 13–23, DOI: 10.1016/j.cattod.2016.03.018.
7 Y. Pan, X. Liu, W. Zhang, Z. Liu, G. Zeng, B. Shao, Q. Liang, Q. He, X. Yuan, D. Huang and M. Chen, *Appl. Catal., B*, 2020, **265**, 118579, DOI: 10.1016/j.apcatb.2019.118579.
8 A. Nasir, S. Khalid, T. Yasin and A. Mazare, *Energies*, 2022, **15**, 6248, DOI: 10.3390/en15176248.
9 N. R. Khalid, A. Majid, M. B. Tahir, N. A. Niaz and S. Khalid, *Ceram. Int.*, 2017, **43**, 14552–14571, DOI: 10.1016/j.ceramint.2017.08.143.
10 D. Wang, N. B. Saleh, W. Sun, C. M. Park, C. Shen, N. Aich, W. J. Peijnenburg, W. Zhang, Y. Jin and C. Su, *Environ. Sci. Technol.*, 2019, **53**, 7265–7287, DOI: 10.1021/acs.est.9b01453.
11 L. G. Devi and R. Kavitha, *Appl. Surf. Sci.*, 2016, **360**, 601–622, DOI: 10.1016/j.apsusc.2015.11.016.
12 L. L. Tan, S. P. Chai and A. R. Mohamed, *ChemSusChem*, 2012, **5**, 1868–1882, DOI: 10.1002/cssc.201200480.
13 Q. Xiang, J. Yu and M. Jaroniec, *J. Am. Chem. Soc.*, 2012, **134**, 6575–6578, DOI: 10.1021/ja302846n.
14 H. Yi, D. Huang, L. Qin, G. Zeng, C. Lai, M. Cheng, S. Ye, B. Song, X. Ren and X. Guo, *Appl. Catal., B*, 2018, **239**, 408–424, DOI: 10.1016/j.apcatb.2018.07.068.
15 J. Peng, W. Gao, B. K. Gupta, Z. Liu, R. Romero-Aburto, L. Ge, L. Song, L. B. Alemany, X. Zhan, G. Gao, S. A. Vithayathil, B. A. Kaipparettu, A. A. Marti, T. Hayashi, J. J. Zhu and P. M. Ajayan, *Nano Lett.*, 2012, **12**, 844–849, DOI: 10.1021/nl2038979.
16 Y. Li, Y. Hu, Y. Zhao, G. Shi, L. Deng, Y. Hou and L. Qu, *Adv. Mater.*, 2011, **23**, 776–780, DOI: 10.1002/adma.201003819.
17 S. Sahu, Y. Liu, P. Wang, C. E. Bunker, K. S. Fernando, W. K. Lewis, E. A. Guliants, F. Yang, W. Jinping and Y. P. Sun, *Langmuir*, 2014, **30**(28), 8631–8636, DOI: 10.1021/la5010209.
18 K. Zhou, Y. Zhu, X. Yang, X. Jiang and C. Li, *New J. Chem.*, 2011, **35**, 353–359, DOI: 10.1039/C0NJ00623H.
19 T. S. Rao, in *Biofouling in Industrial Water Systems*, ed. Z. Amjad and K. D. Demadis, Elsevier, 2015, pp. 123–140, DOI: 10.1016/B978-0-444-63228-9.00006-1.
20 P. M. Ashraf, N. M. Lekshmi, S. Chinnadurai, S. Anjitha, M. Archana, C. M. Vineeth Kumar, K. M. Sandhya and A. P. Gop, *Aquacult. Fish.*, 2022, **8**, 538–543, DOI: 10.1016/j.aaf.2022.01.002.
21 P. Sathe, K. Laxman, M. T. Z. Myint, S. Dobretsov, J. Richter and J. Dutta, *Sci. Rep.*, 2017, **7**, 3624, DOI: 10.1038/s41598-017-03636-6.
22 N. M. Lekshmi, P. M. Ashraf, A. K. Keerthana, S. N. Thomas and L. Edwin, *SN Appl. Sci.*, 2020, **2**, 1–9, DOI: 10.1007/s42452-020-03788-7.
23 X. Ren, X. Wang, X. Yang, M. Hu, H. H. Xie and C. Wang, *Polym. Compos.*, 2023, **44**, 5121–5131, DOI: 10.1002/pc.27478.
24 K. Woan, G. Pyrgiotakis and W. Sigmund, *Adv. Mater.*, 2009, **21**, 2233–2239, DOI: 10.1002/adma.200802738.
25 P. M. Ashraf, C. S. Anjana and N. M. Lekshmi, *Int. Biodeterior. Biodegrad.*, 2024, **193**, 105856, DOI: 10.1016/j.ibiod.2024.105856.
26 S. Sfameni, T. Lawnick, G. Rando, A. Visco, T. Textor and M. R. Plutino, *Nanomaterials*, 2022, **12**, 3404, DOI: 10.3390/nano12193404.
27 E. Richard, R. V. Lakshmi, S. T. Aruna and B. J. Basu, *Appl. Surf. Sci.*, 2013, **277**, 302–309, DOI: 10.1016/j.apsusc.2013.04.052.
28 B. Xu, Z. Cai, W. Wang and F. Ge, *Surf. Coat. Technol.*, 2010, **204**, 1556–1561, DOI: 10.1016/j.surfcoat.2009.09.086.
29 M. R. Plutino, C. Colleoni, I. Donelli, G. Freddi, E. Guido, O. Maschi, A. Mezzi and G. Rosace, *J. Colloid Interface Sci.*, 2017, **506**, 504–517, DOI: 10.1016/j.jcis.2017.07.048.
30 I. Ielo, M. Galletta, G. Rando, S. Sfameni, P. Cardiano, G. Sabatino, D. G. Drommi and M. R. Plutino, *IOP Conf. Ser.: Mater. Sci. Eng.*, 2020, **777**, 012003, DOI: 10.1088/1757-899X/777/1/012003.
31 S. Sfameni, G. Rando, A. Marchetta, C. Scolaro, S. Cappello, C. Urzì, A. Visco and M. R. Plutino, *Gels*, 2022, **8**, 528, DOI: 10.3390/gels8090528.
32 D. B. Hamal, J. A. Haggstrom, G. L. Marchin, M. A. Ikenberry, K. Hohn and K. J. Klabunde, *Langmuir*, 2010, **26**, 2805–2810, DOI: 10.1021/la902844r.
33 B. O. Bica and J. V. S. de Melo, *Constr. Build. Mater.*, 2020, **252**, 119120, DOI: 10.1016/j.conbuildmat.2020.119120.
34 N. F. F. Moreira, M. J. Sampaio, A. R. Ribeiro, C. G. Silva, J. L. Faria and A. M. T. Silva, *Appl. Catal., B*, 2019, **248**, 184–192, DOI: 10.1016/j.apcatb.2019.02.001.
35 P. Devendran, D. Selvakumar, G. Ramadoss, R. Sivaramakrishnan, T. Alagesan, R. Jayavel and K. Pandian, *Chemosphere*, 2022, **287**(1), 132091, DOI: 10.1016/j.chemosphere.2021.132091.
36 X. Wang, K. Ma, T. Goh, M. R. Mian, H. Xie, H. Mao, J. Duan, K. O. Kirlikovali, A. E. Stone, D. Ray and M. R. Wasielewski, *J. Am. Chem. Soc.*, 2022, **144**, 12192–12201, DOI: 10.1021/jacs.2c03060.
37 L. Valenzuela, A. Iglesias-Juez, B. Bachiller-Baeza, M. Faraldos, A. Bahamonde and R. Rosal, *J. Mater. Chem. B*, 2020, **8**, 8294–8304, DOI: 10.1039/D0TB01428A.
38 S. Naz, A. Gul and M. Zia, *IET Nanobiotechnol.*, 2020, **14**, 1–13.

39 A. Banisharif, A. A. Khodadadi, Y. Mortazavi, A. A. Firooz, J. Beheshtian, S. Agah and S. Menbari, *Appl. Catal., B*, 2015, **165**, 209–221.
40 S. Zhan, J. Yang, Y. Liu, N. Wang, J. Dai, H. Yu, X. Gao and Y. Li, *J. Colloid Interface Sci.*, 2011, **355**, 328–333, DOI: 10.1016/j.jcis.2010.11.026.
41 O. F. S. Khasawneh and P. Palaniandy, *Environ. Technol. Innovation*, 2021, **21**, 101230.
42 A. Manivel, S. Naveenraj, P. S. Sathish Kumar and S. Anandan, *Sci. Adv. Mater.*, 2010, **2**, 51–57.
43 X. Peng, M. Wang, F. Hu, F. Qiu, H. Dai and Z. Cao, *J. Alloys Compd.*, 2019, **770**, 1055–1063.
44 R. Gopika, P. M. Ashraf and P. K. Binsi, *Arabian J. Sci. Eng.*, 2023, 1–19, DOI: 10.1007/s13369-023-08569-z.
45 S. V. Gopal, R. Mini, V. B. Jothy and I. H. Joe, *Mater. Today: Proc.*, 2015, **2**, 1051–1055, DOI: 10.1016/j.matpr.2015.06.036.
46 P. Makuła, M. Pacia and W. Macyk, *J. Phys. Chem. Lett.*, 2018, **9**, 6814–6817, DOI: 10.1021/acs.jpclett.8b02892.
47 M. V. Shandrikov, A. S. Bugaev, A. V. Vizir, K. P. Savkin and E. M. Oks, *J. Phys.: Conf. Ser.*, 2018, **1115**, 032055, DOI: 10.1088/1742-6596/1115/3/032055.
48 X. F. Fan and J. M. Liu, *J. Air Waste Manage. Assoc.*, 2015, **65**, 50–58, DOI: 10.1080/10962247.2014.962647.
49 M. Podder, M. F. Ahmed, M. R. Moni, M. L. Rahman, B. Biswas and N. Sharmin, *Arabian J. Chem.*, 2023, **16**, 5.
50 S. Fatima, M. Anwar, A. S. Almalki, A. Alhadhrami, M. F. Warsi and Z. M. El-Bahy, *Ceram. Int.*, 2024, **50**, 29201–29212.
51 P. Borah, D. Siboh, P. K. Kalita, J. K. Sarma and N. M. Nath, *Phys. B*, 2018, **530**, 208–214.
52 A. Sciortino, F. Ferrante, G. Gonçalves, G. Tobias, R. Popescu, D. Gerthsen, N. Mauro, G. Giammona, G. Buscarino, F. M. Gelardi and S. Agnello, *ACS Appl. Mater. Interfaces*, 2021, **13**, 49232–49241, DOI: 10.1021/acsami.1c14299.
53 S. Na-Phattalung, D. J. Harding, P. Pattanasattayavong, H. Kim, J. Lee, D.-W. Hwang, T. D. Chung and J. Yu, *J. Phys. Chem. Solids*, 2022, **162**, 110503, DOI: 10.1016/j.jpcs.2021.110503.
54 J. Huang, S. Wen, J. Liu and G. He, *J. Nat. Gas Chem.*, 2012, **21**, 302–307, DOI: 10.1016/S1003-9953(11)60368-X.
55 M. M. Mohamed, W. A. Bayoumy, M. E. Goher, M. H. Abdo and T. Y. Mansour El-Ashkar, *Appl. Surf. Sci.*, 2017, **412**, 668–682, DOI: 10.1016/j.apsusc.2017.03.200.
56 Y. Li, W. Xiang, T. Zhou, M. Huang, C. Wang, X. Wu, J. Mao and P. Wang, *Chin. Chem. Lett.*, 2020, **31**, 2757–2761, DOI: 10.1016/j.cclet.2020.01.032.
57 F. M. Dukes, E. Iuppa, B. Meyer and M. J. Shultz, *Langmuir*, 2012, **28**, 16933–16940, DOI: 10.1021/la303848g.
58 G. Žerjav, M. S. Arshad, P. Djinović, I. Junkar, J. Kovač, J. Zavašnik and A. Pintar, *Nanoscale*, 2017, **9**, 4578–4592, DOI: 10.1039/C7NR00704C.
59 M. Shaban, A. M. Ashraf and M. R. Abukhadra, *Sci. Rep.*, 2018, **8**, 1–17, DOI: 10.1038/s41598-018-19172-w.
60 M. Kocijan, L. Ćurković, D. Ljubas, K. Mužina, I. Bačić, T. Radošević, M. Podlogar, I. Bdikin, G. Otero-Irurueta and M. J. Hortigüela, *Appl. Sci.*, 2021, **11**, 3966, DOI: 10.3390/app11093966.
61 D. T. Cromer and K. Herrington, *J. Am. Chem. Soc.*, 1955, **77**, 4708–4709, DOI: 10.1021/ja01623a004.
62 S.-C. Yu, J.-S. Lee, S.-F. Tung and C.-L. Lan, *Golden Book of Phase Transitions*, Wroclaw, 2002, vol. 1, p. 1.
63 S.-C. Yu, J.-S. Lee, S.-F. Tung and C.-L. Lan, *J. Geol. Soc. China*, 1999, **42**, 349–358.
64 A. V. Vorontsov and S. V. Tsybulya, *Ind. Eng. Chem. Res.*, 2018, **57**, 2526–2536, DOI: 10.1021/acs.iecr.7b04480.
65 K. J. Mintz, M. Bartoli, M. Rovere, Y. Zhou, S. D. Hettiarachchi, S. Paudyal, J. B. Chen, P. Y. Liyanage, R. Sampson and D. Khadka, *Carbon*, 2021, **173**, 433–447, DOI: 10.1016/j.carbon.2020.11.017.
66 F. Dai, Q. Zhuang, G. Huang, H. Deng and X. Zhang, *ACS Omega*, 2023, **8**, 17064–17076, DOI: 10.1021/acsomega.3c01336.
67 R. Ravinesh, R. L. Laju, J. K. P. Edward and A. Biju Kumar, *J. Aquat. Biol. Fish.*, 2023, **11**, 28–34.
68 L. Chen and P.-Y. Qian, *Mar. Drugs*, 2017, **15**, 264, DOI: 10.3390/md15090264.
69 M. S. Selim, S. A. El-Safty, M. A. Shenashen, S. A. Higazy and A. Elmarakbic, *J. Mater. Chem. B*, 2020, **8**, 3701–3732, DOI: 10.1039/C9TB02119A.
70 S. Mhaddolkar, A. Dineshbabu, T. Sujitha and L. Jayasree, *Int. J. Life Sci.*, 2019, **7**, 655–664.
71 P. M. Álvarez, J. Jaramillo, F. Lopez-Pinero and P. K. Plucinski, *Appl. Catal., B*, 2010, **100**, 338–345, DOI: 10.1016/j.apcatb.2010.08.010.
72 Z. Wu, F. Dong, W. Zhao, H. Wang, Y. Liu and B. Guan, *Nanotechnology*, 2009, **20**, 235701, DOI: 10.1088/0957-4484/20/23/235701.